Geophysical Research Letters

RESEARCH LETTER
10.1029/2025GL115464

Can Traveltime Tomography Benefit From Wave Amplitudes?

Ayon Ghosh[1], Ebru Bozdağ[2], and Jeroen Ritsema[3]

[1]Department of Geophysics, Colorado School of Mines, Golden, CO, USA, [2]Department of Applied Mathematics & Statistics and Department of Geophysics, Colorado School of Mines, Golden, CO, USA, [3]Department of Earth and Environmental Sciences, University of Michigan, Ann Arbor, MI, USA

Key Points:

- Amplitudes can help determine the optimal damping factor in linearized traveltime inversions
- Recorded Sdiff amplitudes are large suggesting ∼1% negative gradient for S waves at the base of the large-low velocity provinces
- Incorporation of 3D wavefield simulations in tomography explains amplitudes better

Supporting Information:

Supporting Information may be found in the online version of this article.

Correspondence to:

A. Ghosh,
ayonghosh@mines.edu

Citation:

Ghosh, A., Bozdağ, E., & Ritsema, J. (2025). Can traveltime tomography benefit from wave amplitudes? *Geophysical Research Letters*, *52*, e2025GL115464. https://doi.org/10.1029/2025GL115464

Received 20 FEB 2025
Accepted 14 AUG 2025

Author Contributions:

Conceptualization: Ebru Bozdağ, Jeroen Ritsema
Data curation: Ayon Ghosh
Formal analysis: Ayon Ghosh
Funding acquisition: Ebru Bozdağ, Jeroen Ritsema
Investigation: Ayon Ghosh, Ebru Bozdağ, Jeroen Ritsema
Methodology: Ebru Bozdağ, Jeroen Ritsema
Resources: Ebru Bozdağ
Supervision: Ebru Bozdağ
Validation: Ayon Ghosh
Visualization: Ayon Ghosh
Writing – original draft: Ayon Ghosh
Writing – review & editing: Ayon Ghosh, Ebru Bozdağ, Jeroen Ritsema

Abstract Regularization of seismic inversions has a strong imprint on tomographic images. We analyze recorded and spectral-element S, Sdiff, and SS waveforms to evaluate the benefit of body-wave amplitudes in global tomography. L-curve analysis for S40RTS models with recorded and synthetic waveforms show that SS-S traveltimes and SS/S amplitude ratios have minima within the same damping parameter range. SS/S ratios for S40RTS and model GLAD-M25 show the trade-off between scale-length and strength of lowermost-mantle heterogeneities. The recorded SS/Sdiff ratios are lower than predicted by 3D mantle models which may be explained by a decrease in the mean shear velocity by ∼1% at the lowermost 200 km of the mantle. Our results suggest that SS/S amplitude measurements made with 3D waveforms can be used to constrain damping in linearized inversions, and amplitudes are essential for studying the size of heterogeneities.

Plain Language Summary Seismic tomography is a powerful technique for imaging 3D Earth's interior and explaining its dynamics. However, "regularization"—choices that steer the numerical process of tomography toward a smooth image of Earth—is a necessary evil because seismic waves crossing in the mantle are uneven and theoretical assumptions are necessary. In this study, we analyze seismic waves, S (the direct shear wave), Sdiff (the core-diffracted shear wave), and SS (the shear wave reflected off Earth's surface) in recorded seismograms and seismograms computed for two 3D mantle models to determine whether wave amplitudes provide usable additional constraints on Earth's 3D structure. We find the SS/S amplitude ratio is sensitive to the scale length of 3D wavespeed variations in the mantle and that a global collection of SS/S measurements can be useful in selecting the optimal regularization level. We also observe that recorded amplitudes of Sdiff waves are larger than the model predictions. This suggests that the shear wavespeed in the lowermost 200 km of the mantle is about 1% lower than documented in standard seismic models, especially beneath Africa and the Pacific Ocean.

1. Introduction

Wave amplitudes are underutilized in seismic tomography but can complement traveltime (i.e., phase) data provided that their nonlinear sensitivity to source, attenuation, and complex propagation effects are properly incorporated (e.g., Dalton & Ekström, 2006; Woodhouse & Wong, 1986). In principle, waveform inversion approaches aim to utilize both amplitude and phase information (e.g., French & Romanowicz, 2014; Karaoğlu & Romanowicz, 2018; Lebedev et al., 2005; Thrastarson et al., 2024). However, in practice, the separation of phase and amplitude helps mitigate the trade-off between seismic parameters linearizing the inverse problem (Bozdağ et al., 2011; Tromp et al., 2005). Thus, even some recent full-waveform inversion (FWI) models are still constructed based on traveltime measurements (Bozdağ et al., 2016; Cui et al., 2024).

Regardless of data types or imaging techniques, global tomographic models of shear wavespeed (v_s) agree on the long-wavelength seismic structure of the mantle (e.g., Boschi, 2003; Ritsema & Lekić, 2020), and provide essential constraints on plate subduction and deep-mantle flow (e.g., Garnero et al., 2016; Goes et al., 2017). However, the short-wavelength (<1,000 km) v_s structure and the strength of v_s variations overall are inconsistently resolved due to unbalanced data coverage and differences in modeling techniques. The inversion is usually stabilized by regularization (e.g., damping or smoothing) in both linearized and full-waveform approaches, which directly affects the characteristics of the tomographic model. The choice of regularization generally depends on the data types used, but any tomographic image includes structures that are not fully constrained by data (e.g., Bozdağ & Trampert, 2010).

This study investigates whether body-wave amplitude measurements can optimize linearized traveltime inversions. It is not our goal to evaluate tomographic modeling choices. Rather, we explore whether independent measurements of body-wave amplitudes can sharpen the minimum of the L-curve for misfit. Following Bozdağ and Trampert (2010), we compute spectral-element synthetics for S40RTS and 16 S40RTS-like models (Ritsema et al., 2011), constructed using the same data set and least-squares inversion scheme but with different damping strengths. In addition, we compute synthetics for 1D PREM (Dziewonski & Anderson, 1981) as reference and the global FWI model GLAD-M25 (Lei et al., 2020). We measure SS-S traveltimes and SS/S amplitude ratios of recorded and synthetic waveforms of S40RTS, using PREM synthetics as reference to explore how amplitudes are affected by damping. We make the same measurements with GLAD-M25 to observe the effect of different tomographic techniques (i.e., ray theory vs. FWI). Additionally, we examine how well current tomographic models explain the mantle, focusing on the D″ region.

2. Models, Data, and Numerical Simulations

We use 3D global mantle models, isotropic S40RTS with its 16 different versions and GLAD-M25 with transverse isotropy in the upper mantle, and 1D isotropic PREM (Dziewonski & Anderson, 1981) as reference in our analysis. GLAD-M25 is an FWI model constructed with multitaper traveltime measurements based on 3D spectral-element simulations taking finite-frequency complexities of wave propagation into account. S40RTS and 16 S40RTS-like models were derived from Rayleigh-wave phase velocity, body-wave traveltime, and normal-mode splitting data. Each S40RTS model is a solution of a linearized, damped least-squares inversion written as $\mathbf{m}^{\dagger} = \mathbf{G}^{\dagger}\mathbf{d}$, where $\mathbf{G}^{\dagger} = \left(\mathbf{G}^{T}\mathbf{G} + \lambda\mathbf{I}\right)^{-1}\mathbf{G}^{T}$ and $\mathbf{G}$ relates the data vector $\mathbf{d}$ to the true model $\mathbf{m}$, which is estimated as $\mathbf{m}^{\dagger}$(e.g., Menke, 1989). The damping, controlled by the factor λ, aims to find a balance between data fit and model appearance. Generally, the model with "weak" perturbations in v_s and with an "acceptable" data fit is deemed preferable. The 17 versions of S40RTS are the results of different values for λ. We quantify the damping by the resolved number of unknowns N, corresponding to the trace of the resolution matrix $\mathbf{G}^{\dagger}\mathbf{G}$. N decreases when the applied damping is stronger (i.e., when λ is larger). We explore values of N, specific to model S40RTS, between 872 (most damping applied) to 15,988 (least damping applied). The data fit as a function of N is colloquially known as the "L-curve." The preferred model is generally selected near its kink. This is at $N = 8{,}112$ for S40RTS. In Figure 1, we present selected depth sections of three S40RTS models and GLAD-M25 for a visual comparison of the impact of damping (see Figures S1 and S2 in Supporting Information S1 for all S40RTS-like models).

We calculate synthetics using PREM and 3D mantle models discussed above with SPECFEM3D_GLOBE (Komatitsch & Tromp, 2002a, 2002b) and compare them with the recorded broadband waveforms downloaded from EarthScope. We use 43 earthquakes from the Global Centroid Moment Tensor catalog (Ekström et al., 2012) (Figure S3, Table S1 in Supporting Information S1) and global and local seismic stations (Table S2 in Supporting Information S1). Hour-long synthetic seismograms with a minimum period of ∼17 s are computed, consistent with the period of body waves used in S40RTS and GLAD-M25 (see Text S1 in Supporting Information S1 for details).

3. Measurements

We analyze two observables: the *traveltime difference* between surface reflections SS and direct S waves, and their *logarithmic amplitude ratios*. These measurements are made for both recorded seismograms and 3D synthetic waveforms, each expressed relative to synthetics computed for the PREM.

We define the SS – S traveltime difference for recorded and 3D synthetics as:

$$\delta T^{ss\text{-}s} = \delta T^{ss} - \delta T^{s} = (T^{ss} - T^{ss}_{PREM}) - (T^{s} - T^{s}_{PREM}). \quad (1)$$

The quantities δT^{ss} and δT^{s} are measured by cross-correlating 80-s windows of transverse-component waveforms centered on the theoretical SS and S traveltimes, respectively.

The amplitude anomaly is defined using the natural logarithm of the RMS amplitude ratios as:

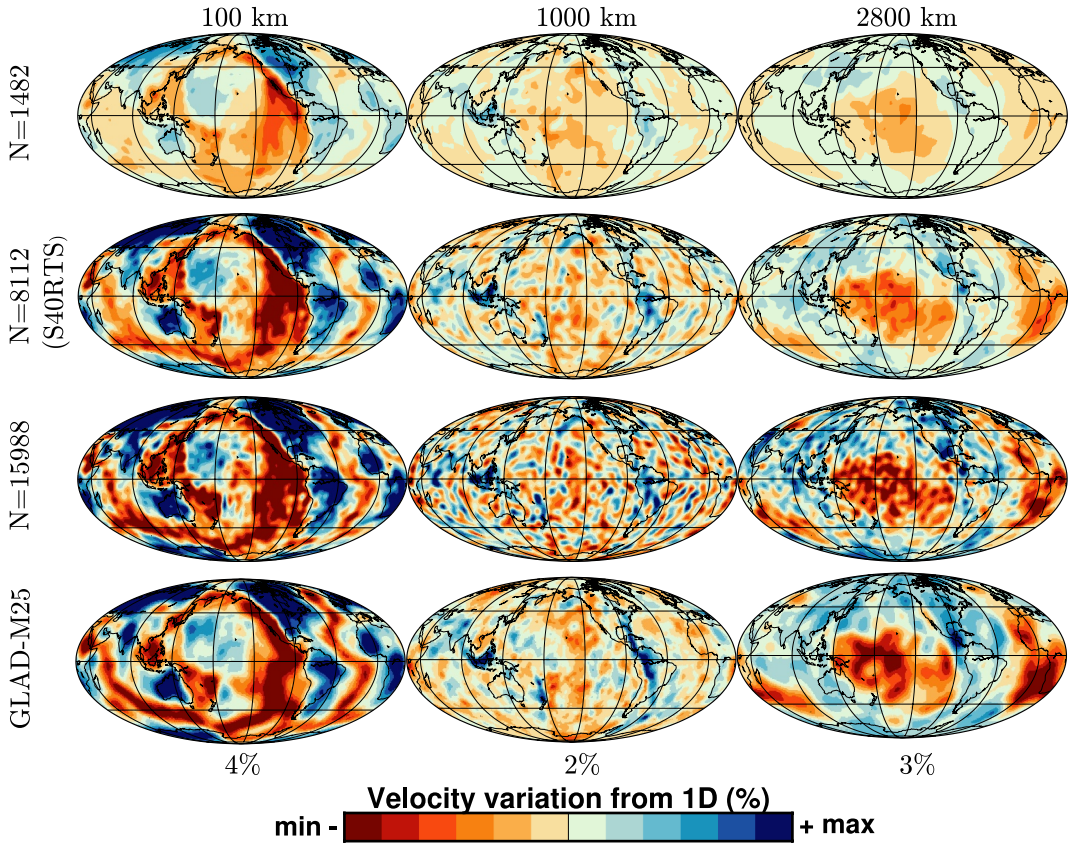

Figure 1. Depth sections of v_s perturbations of S40RTS for $N = 1482$, $N = 8112$, and $N = 15988$, and GLAD-M25.

$$\delta \ln A^{ss/s} = \ln\left(\frac{\langle u^{ss}\rangle}{\langle u^{ss}_{PREM}\rangle}\right) - \ln\left(\frac{\langle u^{s}\rangle}{\langle u^{s}_{PREM}\rangle}\right), \tag{2}$$

where $\langle u^{ss}\rangle$ and $\langle u^{s}\rangle$ denote the root-mean-square amplitudes for SS and S, respectively, from either recorded or 3D synthetic waveforms.

Figure 2 shows the recorded and synthetic SS and S waveforms for a sample earthquake–receiver pair. In this example, PREM underestimates the observed S amplitude by up to a factor of 2.7, the SS amplitude is overestimated by up to a factor of 1.1 in S40RTS and GLAD-M25. SS traveltime misfits are generally within 1 s, though larger than for Sdiff.

To quantify how well a 3D model reproduces the observed anomalies, we define the residual for each source–receiver pair i as:

$$x_i = (\delta T^{ss\text{-}s}_{rec})_i - (\delta T^{ss\text{-}s}_{3D})_i, \tag{3}$$

where $(\delta T^{ss\text{-}s}_{rec})_i$ and $(\delta T^{ss\text{-}s}_{3D})_i$ are the traveltime anomalies from recorded and 3D synthetic waveforms, respectively. Let $\bar{x}$ be the mean residual. The residual variance then is:

$$\sigma^2_{ss\text{-}s} = \frac{1}{n}\sum_i \left(x_i - \bar{x}\right)^2, \tag{4}$$

and the *residual variance ratio*, which expresses the fraction of the variance in the recorded data not explained by the model, is:

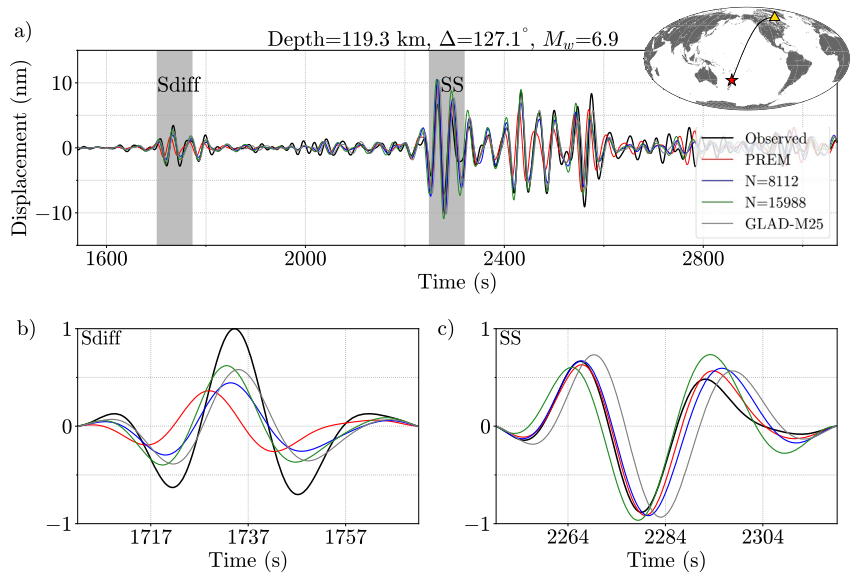

Figure 2. (a) Comparison of transverse component recorded and synthetic waveforms at station CN.FRB of the 5 May 1997 Kermadec Islands earthquake (M_w 6.9; h = 120 km; Δ = 127°). The source-receiver path, earthquake (star) and station (triangle) are shown on the map top-right. (b) and (c) Zoomed-in views of normalized Sdiff (in b) and SS (in c) waveforms. δT^{s} is +5.0 s for the recorded waveform and 4.75, 4.0, 6.25 s for models N = 8112, N = 15916, and GLAD-M25, respectively. $\delta \ln A^{s}$ is 1.1, 0.28, 0.59, and 0.6 for the recorded and the three synthetics. δT^{ss} is −0.75, 0.75, −1.5, and 3.25 s, and $\delta \ln A^{ss}$ is −0.10, 0.07, −0.11, and 0.14. $\delta T^{ss\text{-}s}$ is −4.25, −4, −2.5, and −3 s and $\delta \ln A^{ss/s}$ is −1, −0.22, −0.46 and 0.22, respectively.

$$K^2_{ss\text{-}s} = \frac{\sigma^2_{ss\text{-}s}}{\frac{1}{n}\sum_i \left(\delta T^{ss\text{-}s}_{rec,i} - \overline{\delta T^{ss\text{-}s}_{rec}}\right)^2}. \quad (5)$$

A lower $K^2_{ss\text{-}s}$ value indicates a better match between the recorded and synthetic waveforms. Analogous equations for $K^2_{ss/s}$ can be defined for amplitude anomalies $\delta \ln A^{ss/s}$ following the same logic.

4. Results

Figure 3 shows the residual variance ratios for the S40RTS models, $K^2_{ss\text{-}s}$ and $K^2_{ss/s}$, as a function of N. We divide the measurements into two epicentral distance ranges: 55−110° and 110−140°. In the first range, S waves turn in the lower mantle or diffract briefly along the core-mantle boundary (CMB). In the second range, S diffracts along the CMB for longer distances and is called Sdiff. The shape of $K^2_{ss\text{-}s}$ does not depend on the epicentral distance, but

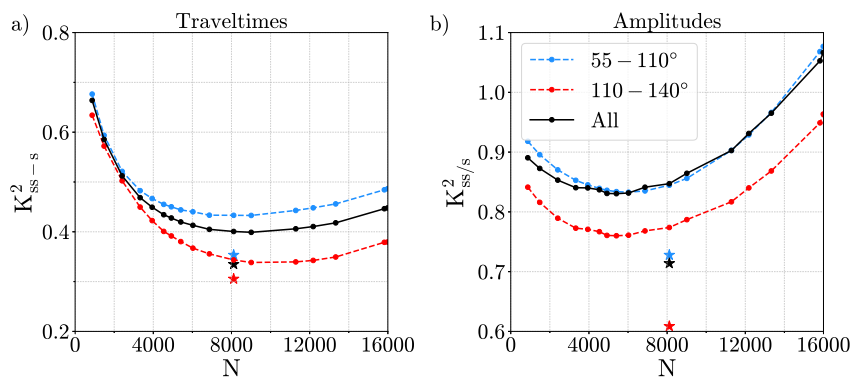

Figure 3. $K^2_{ss\text{-}s}$ (a) and $K^2_{ss/s}$ (b) as a function of N plotted for all distances (in black) and for the epicentral distance ranges 55−110° (in blue) and 110−140° (in red). The values for GLAD-M25 are plotted with stars with corresponding colors.

the residual variance ratios are smallest for long-distance paths, possibly because $\delta T^{ss\text{-}s}$ for SS-Sdiff are larger than the measurement errors.

As expected, the decrease in $K^2_{ss\text{-}s}$ (Figure 3a) resembles the L-curve of Ritsema et al. (2011) constructed based on traveltimes. Model $N = 9,010$ yields the minimum value of $K^2_{ss\text{-}s} = 0.39$ so it explains approximately 60% of the variability in the recorded SS-S traveltimes. The fit to the SS-S traveltimes is significantly worse when $N < 4,000$, that is, for strongly damped models.

Amplitudes are explained more poorly than traveltimes. The minimum of $K^2_{ss/s}$ of 0.82 is obtained for $N = 5,405$ (Figure 3b). In contrast to the SS-S traveltimes, the models with the least damping ($N > 12,000$) explain the SS/S amplitude ratio worse than the strongly damped models ($N < 4,000$). It appears, therefore, that a global collection of SS/S amplitude ratios contains information on the amplitude of the 3D v_s mantle heterogeneities, with the caveat that the fit to SS/S is much lower than the fit to SS-S. $K^2_{ss\text{-}s}$ and $K^2_{ss/s}$ share an overlapping, albeit broad minimum between about $N = 4,000$ and $N = 8,000$. Hence, the choice for $N = 8,112$ from the L-curve analysis of S40RTS is supported by our observations of both SS-S traveltimes and SS/S amplitude ratios.

For comparison, we plotted the GLAD-M25 results with S40RTS at $N = 8,112$. Note that GLAD-M25's resolution is not the same as S40RTS. The long-wavelength v_s perturbations are larger in GLAD-M25 than in S40RTS (Ciardelli et al., 2022) whereas S40RTS has smaller-scale anomalies in the lower mantle. GLAD-M25 explains the SS-S traveltimes better than S40RTS, especially for paths shorter than 110°, likely because it accounts more accurately for the effect on shear waves and the broad SS sensitivity zones in the upper mantle in tomography. GLAD-M25 also better explains the SS/S amplitude ratios, suggesting that body-wave amplitudes are sensitive to the strength of v_s anomalies at long wavelengths. This is also evident in the $K^2_{ss/s}$ curve for S40RTS.

Figure 4 shows the scatter plot of $\delta \ln A^{ss/s}$ values from recorded waveforms with those of the S40RTS and GLAD-M25 synthetics. We grouped the results based on the SS bouncing points as a function of crustal types and Sdiff diffracted through or far from Large Low-Shear-Velocity Provinces (LLSVPs) (Figure S4 in Supporting Information S1) for distances shorter and longer than 110°, respectively. There is no clear pattern for $\delta \ln A^{ss/s}$ measurements for the shorter distance range as a function of the crustal type. We observe predominantly negative $\delta \ln A^{ss/s}$ values for Sdiff propagating through LLSVPs where the correlations decrease significantly. We observe similar patterns for S40RTS and GLAD-M25, where GLAD-M25 correlations with the recorded waveforms are slightly higher (see Figure S5 in Supporting Information S1 for global distribution maps).

In contrast to the lithospheric age expression in $\delta T^{ss\text{-}s}$ (Goes et al., 2013; Woodward & Masters, 1991) (Figure S6 in Supporting Information S1) a geographic pattern in $\delta \ln A^{ss/s}$ is not evident at shorter distances. The recorded values of $\delta \ln A^{ss/s}$ are mostly positive and larger than those predicted by S40RTS and GLAD-M25 at distances shorter than 110°. Zhu et al. (2022) argued that Q_μ is higher than the value in PREM beneath the transition zone based on a study of multiple S-wave amplitudes. The mismatch at shorter distances may also be due to anomalous v_s gradients in the transition zone, which are not captured by 1D reference models. This is consistent with our observation that the SS/S amplitude ratio is high for distances shorter than 80° (Figure 5a) and $\delta \ln A^{ss/s}$ correlates more with the variation in SS amplitudes than S amplitudes (Figures 5b and 5c) in the 55−85° distance range.

$\delta \ln A^{ss/s}$ decreases with increasing epicentral distance and distinctly drops to negative values for distances larger than 120° (Figure 5a). Many of these low values correspond to source-receiver paths with Sdiff traversing LLSVPs in the lowermost mantle. S40RTS and GLAD-M25 do not predict a drop in $\delta \ln A^{ss/s}$ but indicate that, like the data, $\delta \ln A^{ss/s}$ correlates better with the Sdiff amplitudes than the SS amplitude (Figures 5d and 5e). This strongly suggests that the anomalous Sdiff diffraction determines $\delta \ln A^{ss/s}$ for the largest distances. S40RTS and GLAD-M25 synthetics show similar patterns (see Figure S7 in Supporting Information S1) but higher correlations compared to those of recorded waveforms.

We can reproduce the negative values of $\delta \ln A^{ss/s}$ for the largest distances 110° with synthetic seismograms computed for a modified PREM (mPREM) by reducing v_s below ~2,700 km. mPREM is identical to PREM but we reduce v_s up to 1% at the CMB. In mPREM, $v_s = 7.19$ km/s at the CMB compared to $v_s = 7.26$ km/s in PREM. The mean of $\delta \ln A^{ss/s}$ histograms of mPREM is more centered around zero (Figure 6).

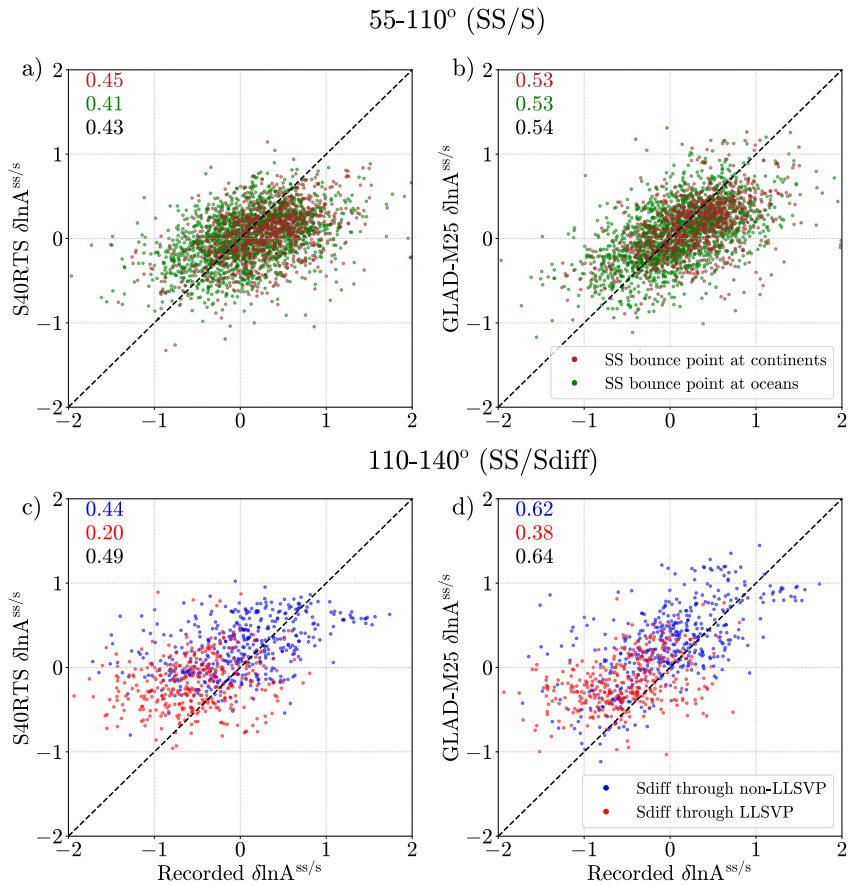

Figure 4. Scatter plots comparing $\delta \ln A^{ss/s}$ values measured from recorded and synthetic waveforms of S40RTS (a, c) and GLAD-M25 (b, d). The measurements are grouped into two epicentral distance ranges: 55°–110° (a, b) and 110°–140° (c, d). For the 55°–110° range, the data are further subdivided based on whether SS bounce points are located beneath oceanic or continental crust. For 110°–140°, the measurements are divided depending on whether Sdiff samples the LLSVPs beneath Africa and the Pacific. Correlation coefficients are shown on the top-left of each plot—colored according to the respective category and in black for the full data set.

5. Discussions and Conclusions

It is expected and encouraging that our analysis of SS-S traveltimes results in the same L-curve analysis by Ritsema et al. (2011). Hence, the analysis of the global traveltime fit does not depend on whether ray theory (as in S40RTS) or 3D numerical wave simulations are used, where the latter address the finite-frequency complexity of wave propagation. It is not unexpected either that S40RTS and GLAD-M25 explain SS/S amplitude ratios more poorly because wave amplitudes depend on seismic parameters nonlinearly, consistent with the study by Bozdağ and Trampert (2010). Only if nonlinearities can be mitigated, amplitudes can provide constraints on the scale and location of elastic heterogeneity as they are sensitive to the gradient of velocity perpendicular to the direction of propagation (Bao et al., 2016; Woodhouse & Wong, 1986). However, the residual variance ratio of SS/S has a minimum, albeit broad, for the moderately damped versions of S40RTS, in the range of $N = 4{,}000$–$8{,}000$. The fit to SS/S deteriorates for the strongly damped cases ($N < 4{,}000$), where the explained variability is reduced by 2%–5% compared to the minimum, and the weakly damped cases ($N > 12{,}000$) show an even worse fit than PREM, confirming body-wave amplitudes contain information on the scale length of heterogeneity (e.g., Tibuleac et al., 2003).

Both GLAD-M25 and S40RTS significantly underestimate Sdiff amplitudes. S40RTS contains smaller-scale v_s heterogeneity than GLAD-M25 but v_s perturbations are larger in GLAD-M25 (see Ciardelli et al. (2022) for power spectra). The scale-length and strength of heterogeneity are likely trading off with each other in D″, that is, larger perturbations or smaller-scale heterogeneities may explain amplitude misfits equally well in LLSVPs. Our

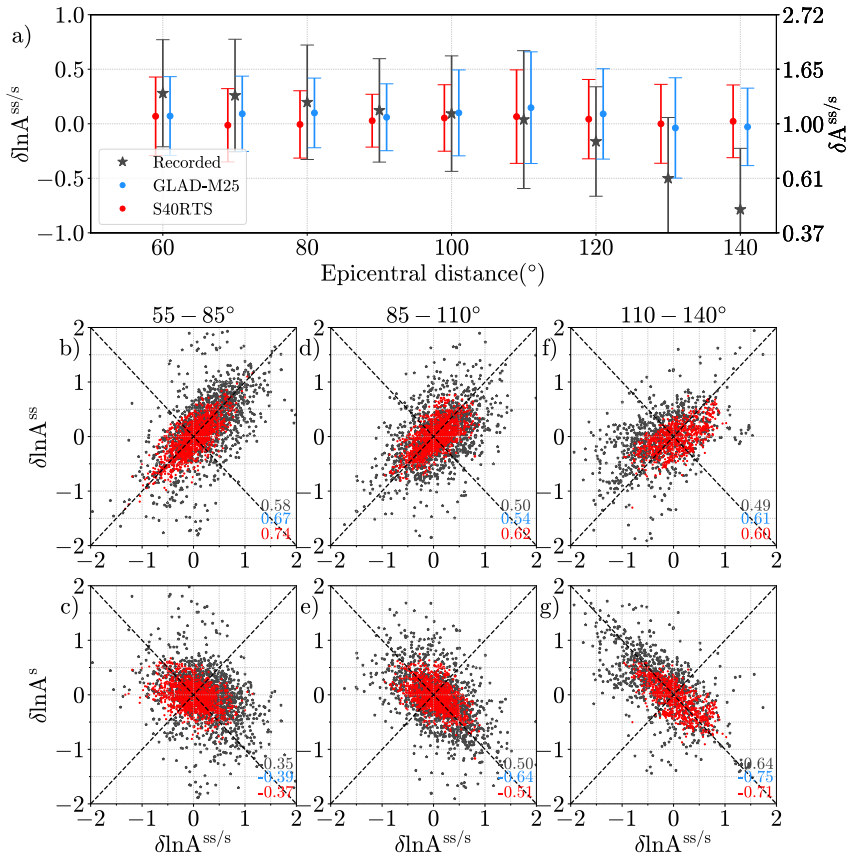

Figure 5. (a) Mean $\delta \ln A^{ss/s}$ with standard deviations at every 10° epicentral bin as a function of epicentral distance for recorded waveforms (black), S40RTS synthetics (red), and GLAD-M25 synthetics (blue). The right axis shows the exponential values of $\delta \ln A^{ss/s}$ measurements. (b–g) Scatter plots of $\delta \ln A^{ss}$ and $\delta \ln A^{s}$ versus $\delta \ln A^{ss/s}$ at the epicentral distance ranges 55–185°, 85–110° and 110–140° for recorded waveforms (black) and S40RTS synthetics (red). The correlation values are displayed at each panel corners with the corresponding colors mentioned above. Scatter plots for GLAD-M25 are shown in Figure S7 in Supporting Information S1.

observations with amplitudes for S40RTS models with varying damping levels (anti-correlation of traveltime and amplitude variances with decreasing damping levels in Figure 3) underscore that amplitude information is essential for improving tomographic mantle models.

However, imaging small-scale heterogeneities and velocity gradients are challenging, specifically with the imperfect global data coverage. Iterative FWI may eventually explain amplitudes if inversions incorporate anelasticity of the mantle and source parameters simultaneously or sequentially with the elastic structure (Fichtner et al., 2024; Valentine & Woodhouse, 2010). Part of our amplitude anomalies could arise from source uncertainties. Our additional tests following To et al. (2016) (see Figures S8 and S9 in Supporting Information S1) show that our results remain the same with perturbations in strike, dip, and rake by 10° from original CMT parameters, and the negative anomalies at the CMB persist even with source perturbations up to 25°. Another source of uncertainties in our observed anomalies may be due to the potential transverse isotropy in the D″ region (Maupin, 1994), which is neglected in S40RTS and GLAD-M25. In this study, we show that the negative amplitude anomalies may be simply explained by the degree-2 lower-mantle elastic structure.

On average, SS/S amplitude ratios decrease by a factor of ∼1.5 at distances larger than 110° when Sdiff propagates far through D″. This trend is mostly driven by the anomalously high amplitudes of Sdiff through the LLSVPs. Variations in attenuation affect body-wave amplitudes (e.g., Liu & Grand, 2018), but due to the strong sensitivity of body-wave amplitudes to scattering (e.g., Bozdağ & Trampert, 2010; Tibuleac et al., 2003), a reduction of v_s with increasing depth in D″ explains both the high amplitudes of Sdiff (and therefore the low SS/S amplitude ratios) and the strong delays of Sdiff through LLSVPs (Ritsema et al., 1997; Thorne et al., 2013). A

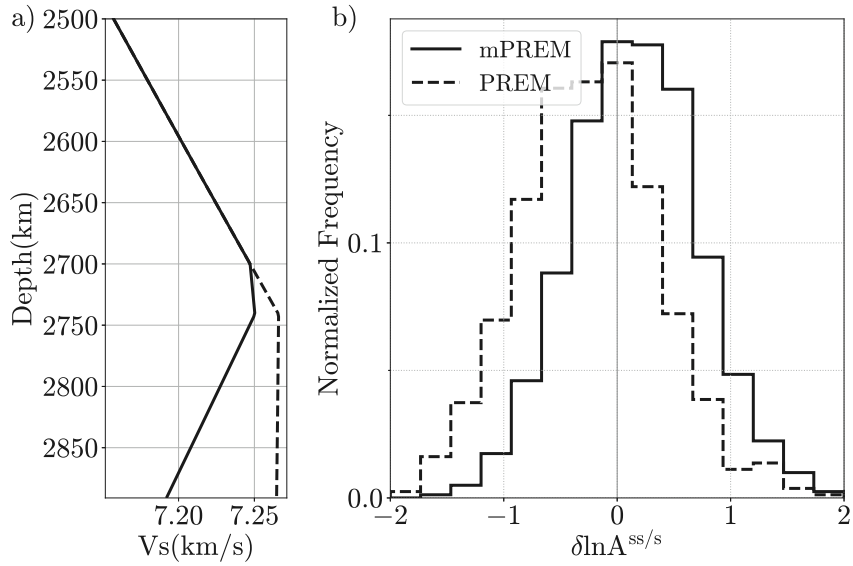

Figure 6. (a) Shear velocity profiles of PREM and its modified version (mPREM) in the lowermost mantle. (b) Histograms of recorded $\delta \ln A^{ss/s}$ measurements relative to PREM and mPREM synthetics for Sdiff waves ($\Delta > 110°$). In these calculations, u_{PREM} in Equation 2 is replaced with synthetic seismograms from mPREM (u_{mPREM}).

negative gradient in v_s is missing in PREM and in STW105 (Kustowski et al., 2008), which are the mean starting models of S40RTS and GLAD-M25, respectively, and may support the thermochemical interpretation of LLSVPs (McNamara, 2019).

Our results indicate the value of independent amplitude measurements from spectral-element seismograms to choose the optimal model from a suite of differently damped models. This approach should be applicable to other tomographic models based on different regularization schemes and is cheaper than iterative FWI. Ultimately, FWI is the way to further improve the resolution of tomographic models in a framework addressing data, source and anelastic parameters properly and self consistently.

Data Availability Statement

The recorded data is available from the EarthScope Consortium (see the list of seismic networks in Table S2 in Supporting Information S1). Due to the size of our synthetic seismograms, we provide the parameter, constants, source, and station files, which were used to generate them with for the reproducibility of our synthetics through Ghosh et al. (2025). We also provide the cross-correlation traveltime and amplitude measurements corresponding to each source-receiver pair through Ghosh et al. (2025). The open-source spectral-element software package is freely available via specfem.org.

Acknowledgments
This research is supported by the National Science Foundation under Award No. EAR-1945565, OAC-2103621 (EB), and EAR-2019379 (JR). The authors acknowledge the Texas Advanced Computing Center (TACC) at The University of Texas at Austin for providing computational resources on "Frontera" system (Stanzione et al., 2020) that have contributed to the research results reported within this paper through allocation EAR21003 (www.tacc.utexas.edu). We thank Computational Infrastructure for Geodynamics (CIG) and the developers for hosting and maintaining . We thank the EarthScope Consortium for maintaining the NSF SAGE data archive (NSF award 1724509), from which the broadband waveforms were obtained. The authors thank the reviewers Barbara Romanowicz and Andrew Valentine and the associate editor Daoyuan Sun for their constructive feedback that greatly improved the manuscript.

References

Bao, X., Dalton, C. A., & Ritsema, J. (2016). Effects of elastic focusing on global models of Rayleigh wave attenuation. *Geophysical Supplements to the Monthly Notices of the Royal Astronomical Society*, *207*(2), 1062–1079. https://doi.org/10.1093/gji/ggw322

Boschi, L. (2003). Measures of resolution in global body wave tomography. *Geophysical Research Letters*, *30*(19). https://doi.org/10.1029/2003gl018222

Bozdağ, E., Peter, D., Lefebvre, M., Komatitsch, D., Tromp, J., Hill, J., et al. (2016). Global adjoint tomography: First-generation model. *Geophysical Journal International*, *207*(3), 1739–1766. https://doi.org/10.1093/gji/ggw356

Bozdağ, E., & Trampert, J. (2010). Assessment of tomographic mantle models using spectral element seismograms. *Geophysical Journal International*, *180*(3), 1187–1199. https://doi.org/10.1111/j.1365-246x.2009.04468.x

Bozdağ, E., Trampert, J., & Tromp, J. (2011). Misfit functions for full waveform inversion based on instantaneous phase and envelope measurements. *Geophysical Journal International*, *185*(2), 845–870. https://doi.org/10.1111/j.1365-246x.2011.04970.x

Ciardelli, C., Bozdağ, E., Peter, D., & van der Lee, S. (2022). SphGLLTools: A toolbox for visualization of large seismic model files based on 3D spectral-element meshes. *Computers & Geosciences*, *159*, 105007. https://doi.org/10.1016/j.cageo.2021.105007

Cui, C., Lei, W., Liu, Q., Peter, D., Bozdağ, E., Tromp, J., et al. (2024). GLAD-M35: A joint p and s global tomographic model with uncertainty quantification. *Geophysical Journal International*, *239*(1), 478–502. https://doi.org/10.1093/gji/ggae270

Dalton, C. A., & Ekström, G. (2006). Global models of surface wave attenuation. *Journal of Geophysical Research*, *111*(B5). https://doi.org/10.1029/2005jb003997

Dziewonski, A. M., & Anderson, D. L. (1981). Preliminary reference Earth model. *Physics of the Earth and Planetary Interiors*, *25*(4), 297–356. https://doi.org/10.1016/0031-9201(81)90046-7

Ekström, G., Nettles, M., & Dziewoński, A. (2012). The global CMT project 2004–2010: Centroid-moment tensors for 13,017 earthquakes. *Physics of the Earth and Planetary Interiors*, *200*, 1–9.

Fichtner, A., Kennett, B. L., Tsai, V. C., Thurber, C. H., Rodgers, A. J., Tape, C., et al. (2024). Seismic tomography 2024. *Bulletin of the Seismological Society of America*, *114*(3), 1185–1213. https://doi.org/10.1785/0120230229

French, S., & Romanowicz, B. A. (2014). Whole-mantle radially anisotropic shear velocity structure from spectral-element waveform tomography. *Geophysical Journal International*, *199*(3), 1303–1327. https://doi.org/10.1093/gji/ggu334

Garnero, E. J., McNamara, A. K., & Shim, S.-H. (2016). Continent-sized anomalous zones with low seismic velocity at the base of Earth's mantle. *Nature Geoscience*, *9*(7), 481–489. https://doi.org/10.1038/ngeo2733

Ghosh, A., Bozdag, E., & Ritsema, J. (2025). Supporting data for Ghosh et al. (2025): Can traveltime tomography benefit from wave amplitudes? *Zenodo*. https://doi.org/10.5281/zenodo.16943429

Goes, S., Agrusta, R., van Hunen, J., & Garel, F. (2017). Subduction-transition zone interaction: A review. *Geosphere*, *13*(3), 644–664. https://doi.org/10.1130/ges01476.1

Goes, S., Eakin, C. M., & Ritsema, J. (2013). Lithospheric cooling trends and deviations in oceanic PP-P and SS-S differential traveltimes. *Journal of Geophysical Research: Solid Earth*, *118*(3), 996–1007. https://doi.org/10.1002/jgrb.50092

Karaoğlu, H., & Romanowicz, B. (2018). Global seismic attenuation imaging using full-waveform inversion: A comparative assessment of different choices of misfit functionals. *Geophysical Journal International*, *212*(2), 807–826. https://doi.org/10.1093/gji/ggx442

Komatitsch, D., & Tromp, J. (2002a). Spectral-element simulations of global seismic wave propagation—I. Validation. *Geophysical Journal International*, *149*(2), 390–412. https://doi.org/10.1046/j.1365-246x.2002.01653.x

Komatitsch, D., & Tromp, J. (2002b). Spectral-element simulations of global seismic wave propagation—II. Three-dimensional models, oceans, rotation and self-gravitation. *Geophysical Journal International*, *150*(1), 303–318. https://doi.org/10.1046/j.1365-246x.2002.01716.x

Kustowski, B., Ekström, G., & Dziewoński, A. (2008). Anisotropic shear-wave velocity structure of the Earth's mantle: A global model. *Journal of Geophysical Research*, *113*(B6). https://doi.org/10.1029/2007jb005169

Lebedev, S., Nolet, G., Meier, T., & Van Der Hilst, R. D. (2005). Automated multimode inversion of surface and S waveforms. *Geophysical Journal International*, *162*(3), 951–964. https://doi.org/10.1111/j.1365-246x.2005.02708.x

Lei, W., Ruan, Y., Bozdağ, E., Peter, D., Lefebvre, M., Komatitsch, D., et al. (2020). Global adjoint tomography—Model glad-M25. *Geophysical Journal International*, *223*(1), 1–21. https://doi.org/10.1093/gji/ggaa253

Liu, C., & Grand, S. P. (2018). Seismic attenuation in the African LLSVP estimated from pcs phases. *Earth and Planetary Science Letters*, *489*, 8–16. https://doi.org/10.1016/j.epsl.2018.02.023

Maupin, V. (1994). On the possibility of anisotropy in the D″ layer as inferred from the polarization of diffracted s waves. *Physics of the Earth and Planetary Interiors*, *87*(1–2), 1–32. https://doi.org/10.1016/0031-9201(94)90019-1

McNamara, A. K. (2019). A review of large low shear velocity provinces and ultra low velocity zones. *Tectonophysics*, *760*, 199–220. https://doi.org/10.1016/j.tecto.2018.04.015

Menke, W. (1989). Discrete inverse theory. *Geophysical Data Analysis*, *289*.

Ritsema, J., Deuss, A., van Heijst, H. J., & Woodhouse, J. H. (2011). S40RTS: A degree-40 shear-velocity model for the mantle from new Rayleigh wave dispersion, teleseismic traveltime and normal-mode splitting function measurements. *Geophysical Journal International*, *184*(3), 1223–1236. https://doi.org/10.1111/j.1365-246X.2010.04884.x

Ritsema, J., Garnero, E., & Lay, T. (1997). A strongly negative shear velocity gradient and lateral variability in the lowermost mantle beneath the Pacific. *Journal of Geophysical Research*, *102*(B9), 20395–20411. https://doi.org/10.1029/97jb01507

Ritsema, J., & Lekić, V. (2020). Heterogeneity of seismic wave velocity in Earth's mantle. *Annual Review of Earth and Planetary Sciences*, *48*(1), 377–401. https://doi.org/10.1146/annurev-earth-082119-065909

Stanzione, D., West, J., Evans, R. T., Minyard, T., Ghattas, O., & Panda, D. K. (2020). Frontera: The evolution of leadership computing at the national science foundation. In *Practice and experience in advanced research computing* (pp. 106–111).

Thorne, M. S., Zhang, Y., & Ritsema, J. (2013). Evaluation of 1-D and 3-D seismic models of the Pacific lower mantle with S, SKS, and SKKS traveltimes and amplitudes. *Journal of Geophysical Research: Solid Earth*, *118*(3), 985–995. https://doi.org/10.1002/jgrb.50054

Thrastarson, S., van Herwaarden, D.-P., Noe, S., Josef Schiller, C., & Fichtner, A. (2024). Reveal: A global full-waveform inversion model. *Bulletin of the Seismological Society of America*, *114*(3), 1392–1406. https://doi.org/10.1785/0120230273

Tibuleac, I. M., Nolet, G., Caryl, M., & Koulakov, I. (2003). P wave amplitudes in a 3-d Earth. *Geophysical Journal International*, *155*(1), 1–10. https://doi.org/10.1046/j.1365-246X.2003.01969.x

To, A., Capdeville, Y., & Romanowicz, B. (2016). Anomalously low amplitude of s waves produced by the 3d structures in the lower mantle. *Physics of the Earth and Planetary Interiors*, *256*, 26–36. https://doi.org/10.1016/j.pepi.2016.04.001

Tromp, J., Tape, C., & Liu, Q. (2005). Seismic tomography, adjoint methods, time reversal and banana-doughnut kernels. *Geophysical Journal International*, *160*(1), 195–216. https://doi.org/10.1111/j.1365-246x.2004.02453.x

Valentine, A. P., & Woodhouse, J. H. (2010). Reducing errors in seismic tomography: Combined inversion for sources and structure. *Geophysical Journal International*, *180*(2), 847–857. https://doi.org/10.1111/j.1365-246x.2009.04452.x

Woodhouse, J., & Wong, Y. (1986). Amplitude, phase and path anomalies of mantle waves. *Geophysical Journal International*, *87*(3), 753–773. https://doi.org/10.1111/j.1365-246x.1986.tb01970.x

Woodward, R. L., & Masters, G. (1991). Global upper mantle structure from long-period differential travel times. *Journal of Geophysical Research*, *96*(B4), 6351–6377. https://doi.org/10.1029/90jb01445

Zhu, M., Sun, S., Zhou, Y., & Wu, Q. (2022). Mantle Q structure from S, SS, SSS and SSSS amplitude measurements. *Geophysical Journal International*, *231*(1), 703–716. https://doi.org/10.1093/gji/ggac217